

# Precise determination of the optical properties of turbid media using an optimized integrating sphere and advanced Monte Carlo simulations. Part 2: experiments

FLORIAN BERGMANN,<sup>1,\*</sup>  FLORIAN FOSCHUM,<sup>1</sup> RALF ZUBER,<sup>2</sup> AND ALWIN KIENLE<sup>1</sup>

<sup>1</sup>Institut für Lasertechnologien in der Medizin und Meßtechnik an der Universität Ulm, Helmholtzstr. 12, D-89081 Ulm, Germany

<sup>2</sup>Gigahertz-Optik, An der Kälberweide 12, D-82299 Türkenfeld, Germany

\*Corresponding author: [florian.bergmann@ilm-ulm.de](mailto:florian.bergmann@ilm-ulm.de)

Received 16 December 2019; revised 21 February 2020; accepted 25 February 2020; posted 26 February 2020 (Doc. ID 385939); published 30 March 2020

Based on theoretical investigations of the light propagation within an integrating sphere, we developed an accurate method to determine the optical properties of scattering media using an integrating sphere-based setup. The method takes into account the exact sphere geometry as well as the different angular distributions of the reflected and transmitted light from the sample and the calibration standard. We tested our novelties successfully in theory with Monte Carlo simulations and in practice using a 3D printed and professionally coated integrating sphere. As a result, we were able to determine precisely the effective scattering coefficient,  $\mu'_s$ , and the absorption coefficient,  $\mu_a$ , between 400 nm and 1500 nm in a range of  $\mu_a = 1e-3 \text{ mm}^{-1}$  to  $10 \text{ mm}^{-1}$  and  $\mu'_s = 0.2 \text{ mm}^{-1}$  to  $100 \text{ mm}^{-1}$ . Usually, the accuracy was around 1% for  $\mu'_s$  and around 3% for  $\mu_a$  for turbid phantom media with an optical thickness  $\tau = \mu'_s d > 1$  and a transmittance signal  $> 0.1\%$ . © 2020 Optical Society of America

<https://doi.org/10.1364/AO.385939>

## 1. INTRODUCTION

Integrating spheres are often used as measurement systems to determine the optical properties of scattering media such as the absorption and the effective scattering coefficients. Besides different configurations for positioning a sample at the sphere's port (inside [1,2] or outside [3]) of a single sphere [4,5] as well as between two spheres [6,7], different radiation or detection configurations and two measurement modes, the substitution and the comparison mode, were reported [3,8,9]. Double integrating spheres are often used in the literature [10–12]. For the evaluation of the measurement signals of double as well as single integrating sphere systems, often the semi-analytical inverse adding doubling algorithm published by Prahl *et al.* [13] is used. Other measurement systems use single sphere setups in comparison mode, and the inverse problem is solved using a numerical Monte Carlo model of light propagation in scattering media [4,14].

In this paper, we investigate the advantages and disadvantages of the proposed setups to develop an optimized measurement system. Based on the theoretical investigations described in the first of these two papers [15], we focus on experimental verifications resulting in a new approach for the precise determination of the optical properties of turbid media using an integrating

sphere. In the present paper, we explain our measurement system, especially the construction of the integrating sphere using a commercial 3D printer similar to [16], the implementation of our measurement method, determination of the hemispherical reflectance coefficient of a mirror as calibration standard, determination of the effective sphere wall reflectance, investigation of the system stability, and the manufacturing of our liquid phantom samples. Subsequently, the validation of the measurement system is presented. We demonstrate the precise determination of optical properties using polystyrene spheres and aluminum oxide nanoparticles as scatterers and trypan blue as an absorber diluted in pure water. In the last section, we point out the effect of a rough sample surface on the determination of  $\mu'_s$  and  $\mu_a$ .

## 2. MEASUREMENT SYSTEM

The integrating sphere setup is based on a 3D printed sphere, a halogen light source, and two spectrometers: one for the predominantly visual (VIS) spectral range from 200 nm to 1100 nm with a spectral resolution of around 3 nm (Maya2000Pro, Ocean Optics, USA) and one for the near-infrared (NIR) spectral range (NIRQuest512-1.7, Ocean Optics, USA) from 900 nm to 1700 nm with a spectral resolution of around 7 nm. The 100 W (Halostar Starlite, OSRAM,



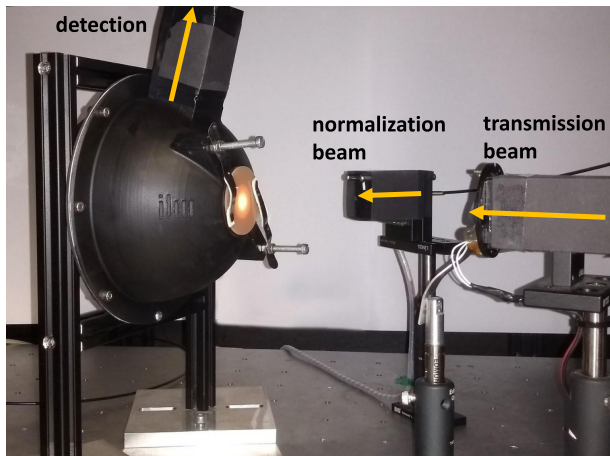


**Fig. 2.** Integrating sphere setup with the 3D printed sphere in side view.

[19,20]. However, for precise determination of the optical properties, it is necessary to consider the different angular distributions of the light reflection and transmission from the sample and the calibration standards. In terms of metrology, it is not accurate to correct the influence of different angular distributions of the light exiting the sample and the calibration standards using only the comparison method or a baffle between sample port and FOV. Rather, the influence of the angular distribution of the light exiting the sample and the calibration standards has to be regarded. For the sample, the angular distribution measured indirectly by the affected total hemispherical reflectance (consisting of volume and surface reflectance) and the affected total hemispherical transmittance signal can be calculated with the radiative transfer equation using, for example, a Monte Carlo method [15]. On the other side, the angular distribution of the reflected light from the calibration standard used in this study is less complex. In the case of a mirror, the distribution is specular contrarily to the commonly used optical polytetrafluoroethylene (OPTFE), e.g., Spectralon or ODM, which has a Lambertian-like distribution.

We decided to use a modification of the substitution method, which corrects, additionally, the change of the sphere throughput applying a normalization beam. Further, with the use of a normalization beam, minor deviations from the ideal Lambertian angular distribution of the sphere wall as well as small changes in the stability of the electrical devices after the initializing and warm-up period are no longer relevant. We tested the dependence of the normalization beam position within the sphere experimentally and found that there is almost no dependence as long as the spot is not too close to any port. Therefore, the normalization beam is orientated so that it hits the sphere wall far away from the ports. The main advantage relative to the comparison method is the separation of sample and calibration standard measurement. Thus, measurements of different samples without a *de novo* calibration procedure are possible. In our case, complete measurements are usually performed in a time span of 2 min. In principle, this allows investigations of dynamic processes such as heating [19,21] or dehydration [22]. Figure 3 depicts the measurement procedure of the used integrating sphere setup, which is implemented in an

automated C++ software routine. The shutter of beam B is on: 1 or off: 0 for the B [reflection, transmission, or normalization] case. The capital letters  $S$ ,  $C^R$ ,  $C^T$ , and  $D$  indicate the measurement object of the measurement sequence. This is the sample  $S$ , the reflectance calibration standard  $C^R$ , air as the transmittance calibration standard  $C^T$ , as well as the dark  $D$ . The lowered indices clarify the illumination configuration: RB for reflection beam, TB for transmission beam, and NB for normalization beam, represented in Fig. 1. Our measurement setup is shielded from ambient light. Thus, the measurement procedure is optimized such that only one dark measurement is needed. Due to possible external stray light in the reflection beam illumination, we recommend using a separate dark measurement for the reflection measurement. For this, the light that passes through the open sample port is absorbed by a light trap. The measurement procedure has to be extended if no shielding of the setup is used. For the start of the integrating sphere measurement, the light source is switched on and the spectrometers are connected and initialized. After a duration of about 30 min, which ensures a constant temperature of the light source and the spectrometers, the measuring procedure starts with the calibration procedure. First, the reflectance calibration standard  $C^R$ , e.g., a mirror, is attached to the sample port, the optimized integrating time used for all measurements is determined, and the sphere throughput  $C_{NB}^R$  is measured using the normalization beam B[0,0,1]. Subsequently, the beam changes to B[0,0,1], and the setup performs the measurement of the reflectance calibration standard  $C_{RB}^R$ . Then, the sample port is emptied and the dark signal,  $D_{RB}$ , is measured in reflection B[0,0,1] using the sample beam switched on. As mentioned before, this additional dark measurement is used to correct for possible external stray light due to the reflection beam, which penetrates through the sphere. After the dark measurement,  $D$ , with B[0,0,0], the transmittance calibration standards  $C_{TB}^T$  and  $C_{NB}^T$  are measured using the transmission B[0,0,1] and the normalization beam B[0,0,1], both with an opened sample port. For the measurements on the sample, one has to align the sample at the sample port, and the signals  $S_{RB}$ ,  $S_{TB}$ , and  $S_{NB}$  are measured for the reflection B[0,0,1], transmission B[0,0,1], and normalization B[0,0,1] illumination, respectively. With regard to the hemispherical reflectance coefficient  $\rho_{cal}$  of the calibration standard, the total hemispherical reflectance  $R$  and the total hemispherical transmittance  $T$  measurements, which are influenced by the port openings and the angular distribution of the calibration standard, can be obtained. As explained in Ref. [15], the optical properties are subsequently determined by a two-dimensional interpolation algorithm comparing  $R$  and  $T$  of an analytical corrected and inverted look-up table (LUT) with the measurement. The LUT has to be calculated in a previous step by a Monte Carlo model using an appropriate refractive index, asymmetry factor, sample thickness, and a suitable subdivision in the optical properties  $\mu'_s$  and  $\mu_a$ . Subsequent to the simulation of the reflected and transmitted signal, we corrected the obtained values with an analytical model of the integrating sphere considering the effective sphere wall reflectance, port losses, and the part of the signal that directly illuminates the detector resulting in an effective reflected and transmitted signal, as explained in Ref. [15].

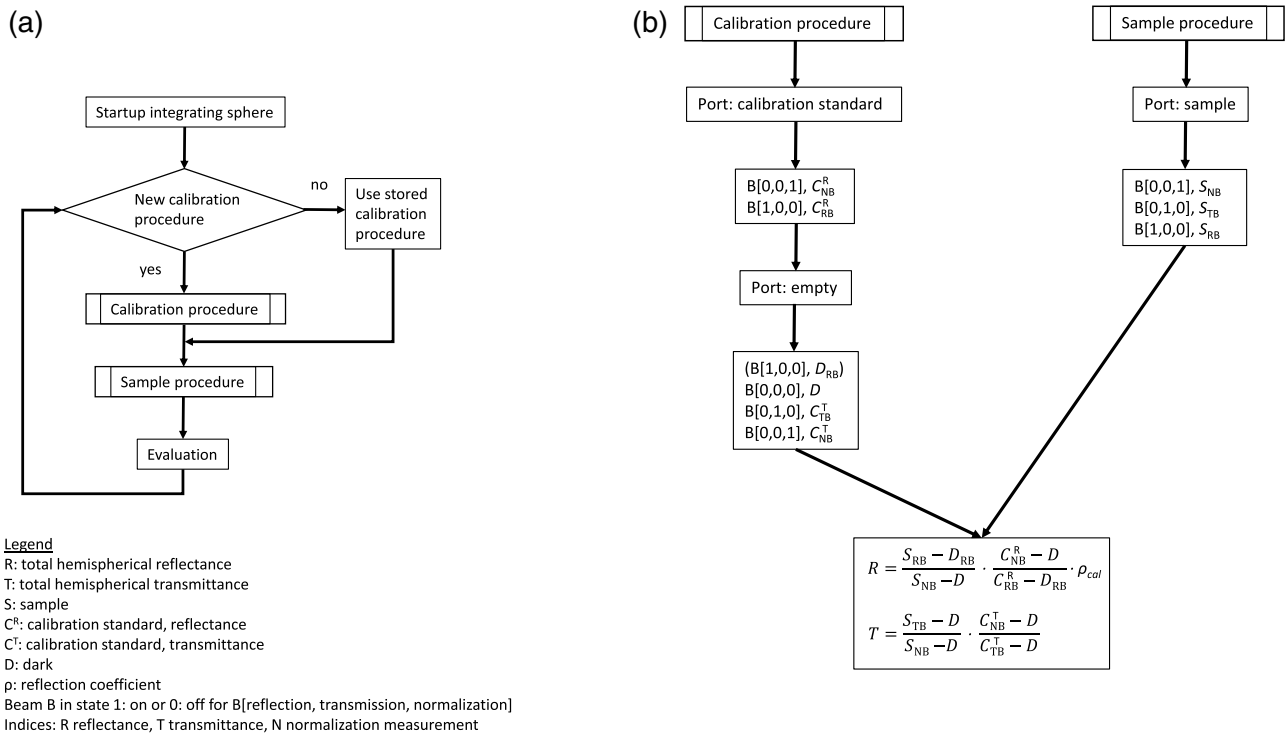


**Fig. 3.** Measuring procedure flowchart (a) with a detailed description (b). Beam B in state 1: on and 0: off for [reflection, transmission, normalization beam].

**C. Calibration Standard**

In our case, besides the hemispherical reflectance coefficient  $\rho_{cal}$  of the calibration standard, also the angular distribution of the reflected light is important. OPTFE has a nearly Lambertian radiation characteristic, but the exact angular distribution of the reflected light is usually unknown. Further drawbacks are that the hemispherical reflectance coefficients of the standard are affected due to aging and damaging of its soft surface. A minor drawback is the non-infinitely large volume scattering, which causes side losses, especially for small port diameters. Therefore, we used a high reflective mirror (68-333, Edmund Optics, USA) as the reflectance calibration standard. Due to the defined specular reflection of the mirror, one can easily determine the hemispherical reflectance coefficient using an intensity measurement of the surface reflectance relative to the incident intensity, illustrated in Fig. 4. The mentioned conventional mirror is surface coated. We added a cover glass layer of finest optical grade glued with epoxy resin to ensure a protective layer to prevent possible surface scratches. The mirror is illuminated under  $5^\circ$  with a diameter of around 5 mm having a small numerical aperture of  $NA \approx 0.06$  according to the illumination beam of our integrating sphere measurement setup, described in Section 2. The surface reflectance is detected via an integrating sphere having a small port diameter. To enable an absolute measurement of the hemispherical reflectance coefficient of the sample (mirror), a reference (air) and a dark measurement are necessary (compare Fig. 4). For both measurements, the same sample or reference to a detector distance of 150 mm was used. Figure 5 depicts the obtained hemispherical reflectance coefficient versus wavelength of the prepared mirror. We used

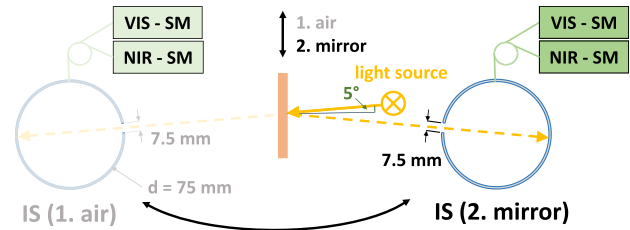


**Fig. 4.** Determination of the hemispherical reflectance coefficient  $\rho_{cal}$  of a mirror. Left, measurement of the incident intensity (1. air) and, right, measurement of the surface reflectance (2. mirror) are shown. SM, spectrometer.

a 20th-degree polynomial fit for smoothing our determined hemispherical reflectance coefficient. The reflectance of the mirror is in the VIS at 500 nm around 98.5% and decreases to 97.5% in the NIR at 1500 nm.

**D. Determination of the Effective Sphere Wall Reflectance**

Several approaches to determine the sphere wall reflectance using an integrating sphere measurement, for example, with (1) a plate coated identically as the sphere wall (removable cap method) [23] or (2) the swiveling of the reflection beam between calibration standard and sphere wall, similar to [10], are conceivable but in case 1, the plate is often not available, and in case 2, the location of the direct radiation may affect the measurement due to inhomogeneities in the coating, as was the case for our setup. Alternatively, one can determine the ratio of

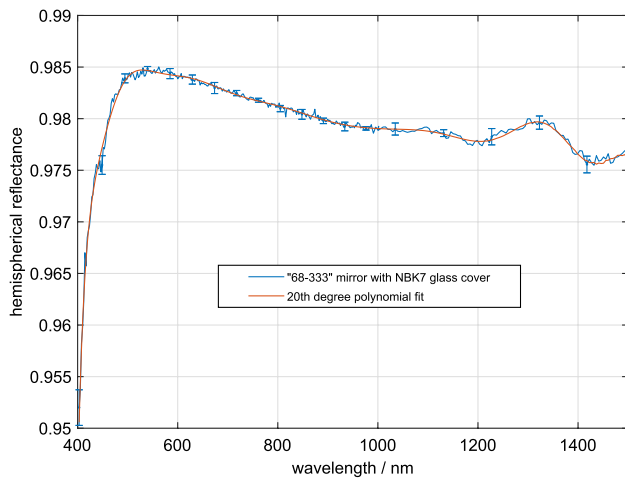


**Fig. 5.** Measurement of the hemispherical reflectance coefficient  $\rho_{\text{cal}}$  as a function of the wavelength for the “68-333” mirror with glass cover of finest optical grade and a 20th-degree polynomial fit of the measurement.

the sphere throughput for an open sample port to a covered one using a calibration standard of known hemispherical reflectance coefficient by illuminating an arbitrary position of the sphere wall. For this, the illumination position remains the same for both configurations. The procedure was performed using the mirror as well as a SRS-99-010 Spectralon. Comparing the ratio of the sphere throughput to our analytical theory gives us the effective sphere wall reflectance, which is similar for both calibration standards (see Fig. 6). Furthermore, we tested a second OPTFE (OPTFE 2) which originates from the same manufacturing batch as the first one (OPTFE 1) but was processed abrasively with a silicon carbide waterproof grinding paper (P240, Buehler, USA) due to surface irregularities from previous improper handling. Nevertheless, the effective sphere wall reflectance is not affected by this. Minor deviations for wavelengths shorter than 500 nm and longer than 1100 nm between the mirror and the OPTFEs can be found. This is possibly caused by the very poor spectral resolution of the hemispherical reflectance coefficient of the Spectralons, given by Labsphere.

In the analytical model, the calibration standard was illuminated diffusely, but the hemispherical reflectance coefficient of the mirror was measured under  $5^\circ$ . To investigate the impact of this issue, we analytically estimated, using Fresnel’s equations, the deviation of the hemispherical reflectance coefficient for silver (complex refractive index from [24]), illuminated at  $5^\circ$  relative to its surface normal compared to a diffuse illumination integrating over the half-space. We found a relative deviation of around 0.05% in the spectral range from 400 nm to 1500 nm. The hemispherical reflectance coefficient of the mirror measured using a  $5^\circ$  illumination therefore does not have a relevant effect on the determination of the effective sphere wall reflectance. Thus, the measured sphere wall reflectance, obtained in this way, is an effective value, which takes inhomogeneities caused by the sphere coating, e.g., at the connection of the two half-spheres, and imperfections such as impurities or the real angular sphere wall distribution into account.

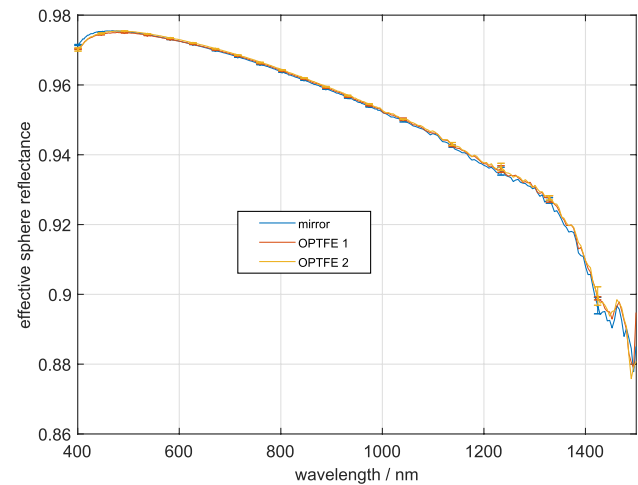


**Fig. 6.** Measurement of the effective sphere wall reflectance versus wavelength. We obtain similar results for the effective sphere wall reflectance using both a Lambertian and a specular surface.

## E. System Stability

We implemented six experimental corrections to obtain precise experimental  $R$  and  $T$  values. First, we used a warm-up of the electrical devices to stabilize the system so that only slow, in a time span of several minutes, and small relative changes  $< 0.1\%$  in the measured signal arose. Using a normalization beam for the measurement of the sphere throughput enables the correction of remaining slow changes (implicitly). Second, to correct for the dark current of the spectrometers as well as the ambient light, we subtracted the dark signal from the associated measurements. Third, the internal stray light in the spectrometers was regarded as an offset. We used different long-pass filters as well as filters with small wavelength bands in the VIS to examine the internal stray light in the spectrometer quantitatively. As a first approximation, we assume that the internal stray light is constant over the entire pixel array. Therefore, we subtract the internal stray light intensity from each spectrum, measured at the spectral border of each spectrometer (VIS: from 220 nm to 300 nm, NIR: from 1500 nm to 1585 nm) for the whole spectral range. In more detail, we used a wavelength range from 220 nm to 300 nm, at which the radiation of the used halogen lamp is negligible, to measure the internal stray light for the VIS spectrometer. For the NIR, we blocked the detection from 1500 nm to 1585 nm using a short-pass filter (84-654, Edmund Optics, USA) between the NIR spectrometer and the detection fiber. For a more precise correction, the internal stray light could be measured in advance for each wavelength. Further on, the high readout noise of the NIR spectrometer prompted us to use fewer repeating measurements. Instead, a longer integrating time was used. The dynamic range of 15000:1 coupled to a 16-bit A/D converter of the InGaAs detector enables the use of measurement with  $N$  times, usually 150, higher integration time than for the VIS spectrometer, whereas for the VIS spectrometer, an averaging over  $N$  spectra is applied at the same time. This keeps the measurement time-synchronous for the parallel use of both spectrometers. Finally, we found a higher deviation from linearity measuring the intensities for different integrating times compared to using the same acquisition time (both using



**Fig. 7.** Empty sample cuvette is shown on the left, whereas the almost closed cuvette filled with a liquid phantom is shown on the right.

the nonlinearity correction from Ocean Optics). Thus, we performed all measurements at equal integrating times.

### F. Sample Preparation

The ideal sample geometry for our integrating sphere measurement is a cylindrical slab with plano-parallel end faces and high surface quality. Furthermore, the lateral dimension of the sample should be larger than the sample port diameter. As for powders and fluid samples, cuvettes are necessary; the exact thickness of the bonding glass, thickness of the sample, as well as the refractive index of the glass slides are required and have to be considered spectrally resolved. We used 3D printed and, subsequently, polished plano-parallel hollow rings made of polylactic acid filament having an inner diameter of 35 mm and different thicknesses as a spacer between two N-BK7 glass slides (34-427, Edmund Optics, USA) (see Fig. 7). Due to the manufacturing process of the N-BK7 glass slides, different batches have different thicknesses and slightly different refractive indices. We measured the thickness of the glass slides as well as of the sample for each configuration with a micrometer gauge. For the spectrally resolved refractive index of the glass slides, the dispersion of the N-BK7 glass given by SCHOTT was used. To fill the cuvette, the spacer was placed on one glass layer, and after the filling of the sample, one can slide the second glass sideways over the chamber to prevent air bubbles in the case of liquid samples. The adhesion between media and glass slides was strong enough to prevent separation for samples having a low vapor pressure.

### 3. VALIDATION

The experimental validation of the integrating sphere setup was done with liquid phantoms based on water (Aampuwa, Fresenius Kabi, Germany), molecular absorbers, and highly scattering aluminum oxide nanoparticles with a mean diameter of 200 nm as well as polystyrene spheres with a mean diameter of 2.74  $\mu\text{m}$ . The advantage of using liquid phantoms in cuvettes

is the high surface quality of the samples through the use of glass slides and the homogeneity of the samples. To prevent agglomeration and adhesion of the scattering particles, we used transparent detergent (Zitrone & Aloe Vera Hand-Spülmittel, Ecover, Belgium) including 5%–15% anionic surfactants with a concentration of about 0.1 vol%. The samples were treated for 20 min with ultrasound before each measurement and in the case of the polystyrene spheres also before the fabrication of certain dilutions. For the evaluation of the integrating sphere measurement, we used the Henyey–Greenstein scattering phase function with appropriate asymmetry factor, specified in the following section.

### A. Validation with Polystyrene Particles Using Mie's Theory

The use of polystyrene spheres has advantages compared to the use of non-spherically shaped aluminum oxide nanoparticles. Besides the spherical shape that can be used for theoretical verification applying Mie's theory, the refractive index of the particles is known from different publications [25–27]. For our first validation, we used polystyrene spheres with a diameter of  $2.74 \mu\text{m} \pm 0.05 \mu\text{m}$  having a concentration of 10 vol% in water (PS-F-B1267, microParticles GmbH, Germany). Besides integrating sphere measurements, also collimated transmittance measurements using a separate setup were performed for a comparison of the scattering coefficients ( $\mu_s$  and  $\mu'_s$ ) with Mie's theory. The applied collimated transmittance setup is an improved version of the setup described by Michels *et al.* [28] and Stocker *et al.* [29]. A small portion of the divergent radiation of the broadband light source (HL 2000 FHSA, Ocean Optics, USA) is coupled into a 100  $\mu\text{m}$  diameter low-OH multimode fiber having an NA = 0.22 (see Fig. 8). The light that passes through the fiber is collimated using an 80 mm achromatic lens positioned at a distance of the focal distance. Two apertures are used before and after the collimation lens. The first aperture is used to reduce the numerical aperture of the fiber in order to prevent illumination of the lens mounting to avoid external stray light. The second aperture reduces the beam size of the collimated beam to about 5 mm in diameter. The light that is not scattered in the sample is detected in the Fourier plane of the achromatic detection lens ( $f = 50 \text{ mm}$ ) with a multimode fiber having an NA = 0.39 and a diameter of 200  $\mu\text{m}$ . The detection fiber is mounted on an  $x - y$  stage to correct a possible displacement of the beam induced by a nonparallel sample or reference surface. The 200  $\mu\text{m}$  detection fiber is used for an easier adjustment. Before coupling in the spectrometer, we used a coupling of the 200  $\mu\text{m}$  detection fiber into a 1000  $\mu\text{m}$  spectrometer fiber with diffusing paper in between. The advantage compared to the previous collimated transmittance setup is the reduced path

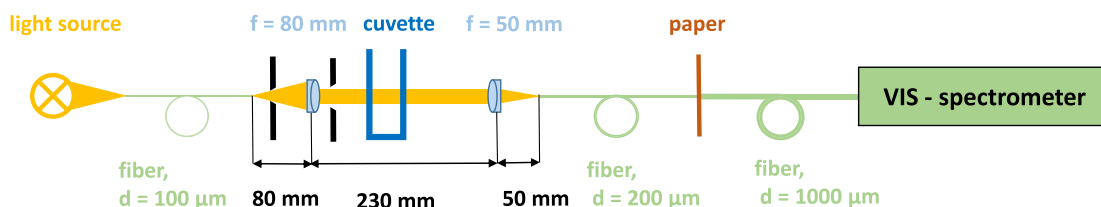


**Fig. 8.** Collimated transmittance setup applying a Fourier plane detection arrangement.

length and the smaller influence of strong forwarded scattered light by using a smaller angle of acceptance of around  $0.23^\circ$ . For the collimated transmittance measurement of the polystyrene spheres, adequate samples were prepared. We used three concentrations between  $c = 0.01$  and  $0.03$  vol%, each in water containing detergent. The samples were filled in a commercial cuvette (QS 10 mm, Hellma, Germany) with a sample thickness of 10 mm, and each measurement was repeated three times by refilling the cuvette. For the integrating sphere measurement, we used a polystyrene sphere concentration of  $c = 0.89$  vol% diluted in water with 0.1 vol% detergent. The exact volume concentration was determined by dehydration of the polystyrene sphere sample achieving a relative accuracy better than 0.1%. The sample was filled in a cuvette of N-BK7 glass slides as described in Section 2.F with a sample thickness of around 4 mm. Three repetitions of the measurements at different sample positions were performed. The results were also compared to three measurements of identical sample refilling the cuvette between each measurement (not shown here). We found that for homogeneous samples, the uncertainties of measurements on different positions or with refilled cuvettes were comparable.

The evaluation of the collimated transmittance measurement was performed with the Beer–Lambert law. Water mixed with 0.1 vol% detergent was used as a reference. The resulting single scattering coefficient  $\mu_s$  can be found in Fig. 9(a) showing the characteristic Mie oscillations, which are caused by constructive and destructive interferences of light scattered by the beads. Compared to Mie's theory using the diameter of the scattered particles given by the manufacturer and the refractive index reported by Ref. [25], we found a shift of the small oscillations in the measurement to smaller wavelengths as well as a 1.5% higher amplitude. The obtained standard deviation was about 0.5%. For the evaluation of the integrating sphere measurements, we used the refractive index of water given by Kedenburg *et al.* [30] and an asymmetry factor of  $g = 0.9$ , which is the mean asymmetry factor ( $g = 0.904 \pm 0.038$ ) of the whole wavelength range for the polystyrene spheres calculated with Mie theory. Due to the relatively large optical thickness of the used samples, we expect errors of below 1%. The obtained  $\mu'_s$  and  $\mu_a$  values are also shown in Fig. 9. Similar to the single scattering coefficient, we found a wavelength shift as well as an absolute deviation in  $\mu'_s$  compared to Mie theory, as described above.

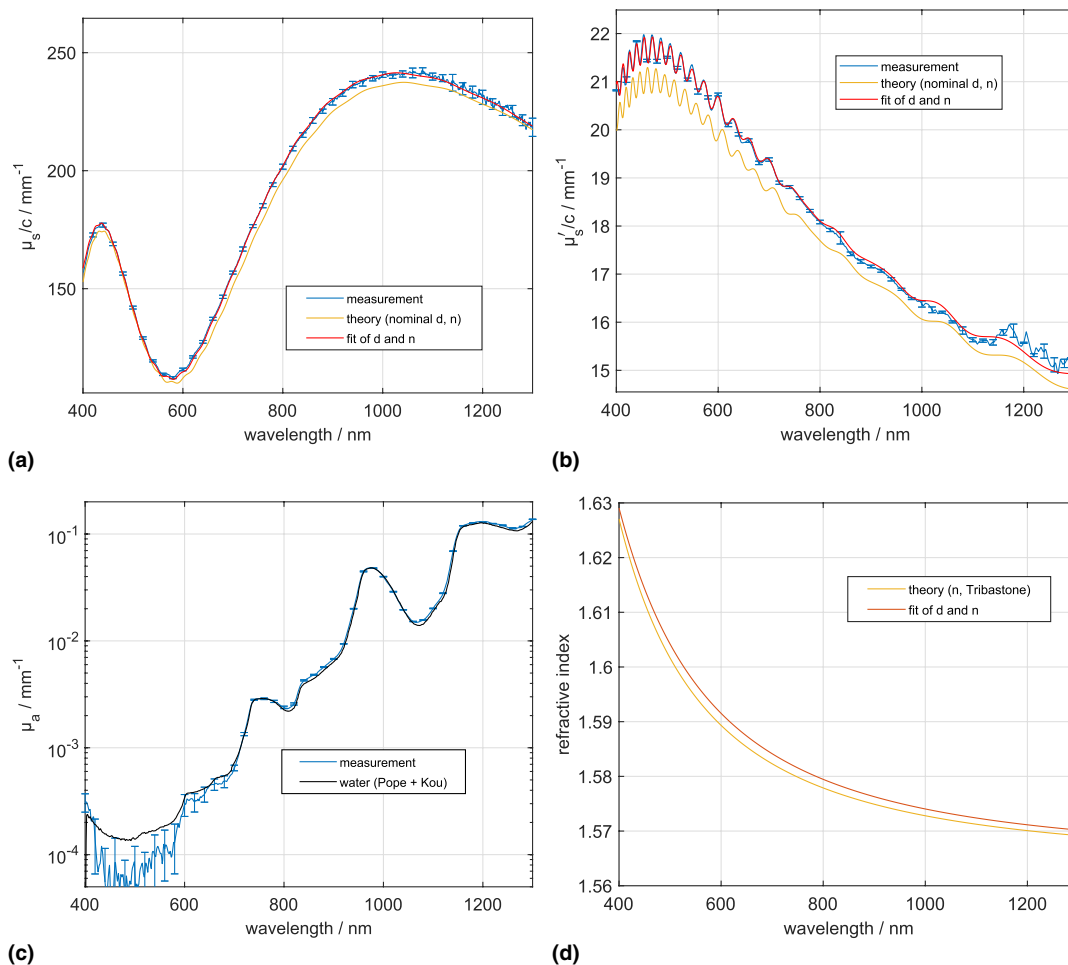


**Fig. 9.** Optical properties of the polystyrene spheres having a diameter of nominal  $2.74 \mu\text{m} \pm 0.05 \mu\text{m}$ , which were mixed in water containing around 0.1 vol% detergent. Besides the integrating sphere setup, also the collimated transmittance setup was used for the measurements. Mie's theory was applied by using the size distribution of the manufacturer and the refractive index (d) by Tribastone and Peck [25]. Fitting the sphere diameter ( $d = 2.696 \pm 0.03 \mu\text{m}$ ) as well as the refractive index of Mie theory enabled an excellent agreement of the optical properties  $\mu_s$  (a) and  $\mu'_s$  (b) at the same time. The absorption coefficient (c) was compared to the literature from Pope *et al.* [32] and Kou *et al.* [31].

The standard deviation between the different measurements for  $\mu'_s$  is below 0.5% and for most  $\mu_a$  values below 2% in the VIS and NIR ranges. Relative high standard deviations occur for  $\mu_a < 1e - 3 \text{ mm}^{-1}$ , which is the measurement limitation of our setup for the used cuvette thickness due to measurement and numerical uncertainties. The spectral range between 1300 nm and 1500 nm is not shown because of the small transmittance due to the high water absorption in combination with the used sample thickness. A small discrepancy in  $\mu_a$  between 800 nm and 950 nm and between 1050 nm and 1150 nm compared with the water absorption of Kou *et al.* [31] (700 nm to 1300 nm) at room temperature was found. Unfortunately, the literature for water absorption determined by various authors gives different values. Nevertheless, comparing possible  $\mu_a$  values from the literature, we found the best match with the absorption coefficient given by Pope *et al.* [32] (400–700 nm) in the VIS and Kou *et al.* in the NIR. We found an excellent agreement between Mie's theory and the experimental values of the two independent scattering coefficients by fitting the refractive index and the size distribution of the beads at the same time. The fitted size distribution is  $d = 2.696 \pm 0.03 \text{ }\mu\text{m}$ , and the refractive index is 0.14% higher at 600 nm compared to the literature [25]. The dispersion for  $\lambda = 400 \text{ nm}$  to  $1300 \text{ nm}$  is given with the first term of Sellmeier's equation as

$$n = \sqrt{1 + \frac{B_1 \cdot \lambda^2}{(\lambda^2 - C_1)}}$$

with  $\lambda$  in  $\mu\text{m}$  and the coefficients  $B_1 = 1.4482367e + 00$  and  $C_1 = 1.9929888e - 02$ . The slight change in the size distribution and the refractive index of the beads yields an excellent agreement of measurement and theory (see Fig. 9).

**B. Validation of the Dynamic Range Using Nanoparticles and Trypan Blue**

We validated the dynamic range of the measurement system with different concentrations of the molecular absorber trypan blue (L6323, Biochrom AG, Germany), which is available in 0.5 vol% saline, aluminum oxide nanoparticles (NO-0050, ioli-tec, Germany) with an average diameter of 200 nm in water, in which the transparent detergent was added. The nanoparticles were used as scatterers having excellent homogeneity after

a 20 min ultrasonic treatment. Long-term measurements of the nanoparticle samples without stirring showed a systematic decrease of around 0.5% in  $\mu'_s$  in the VIS range, 40 min after the treatment. We note that the nanoparticles are cheaper than the often-used polystyrene spheres, and thus they are especially appropriate for making samples with large scattering coefficients and large volumes. We prepared different concentrations of trypan blue between 1.3e-5 vol% (P2) and 0.013 vol% (P6) with a similar amount of nanoparticles (1e-3 vol.%) having an effective scattering coefficient of around  $\mu = 1 \text{ mm}^{-1}$  at 600 nm. For P1, no absorber was added. As described above, we used a self-made cuvette applying N-BK7 glass slides with a sample thickness of around 4 mm and performed three repetitive measurements at different sample positions. For the evaluation of the integrating sphere, the refractive index of water given by Kedenburg *et al.* [30] and an approximated asymmetry factor of  $g = 0.95$  were used. The high asymmetry factor was obtained by use of the equation  $g = 1 - \mu'_s / \mu_s$  and results from further investigations using aluminum oxide in water samples measured with the integrating sphere and the collimated transmittance setup. In Fig. 10, the absorption coefficients of the six phantoms containing different amounts of trypan blue are shown. The absorption of trypan blue dominates in the VIS spectral range, and the increase in absorption according to the used increasing concentrations of the absorbers can be seen. In the NIR spectral range, the water absorption dominates and remains unchanged, as its concentration does not change significantly. The absorption of the pure (0.5 vol% saline) trypan blue was measured in advance with the collimated transmittance setup and then compared with the results of the integrating sphere method. The results were divided therefore by the volume concentration of trypan blue. For all phantoms, a good agreement with errors less than 3% was achieved. Only the sample P2 with the smallest trypan blue concentration differed more for  $\lambda > 700 \text{ nm}$ . Note that we could not find any crosstalk between  $\mu_a$  and  $\mu'_s$  despite the relatively high absorption coefficient. This indicates a good separation of  $\mu'_s$  and  $\mu_a$ . Indeed, the effective scattering coefficient calculated for the stock is consistent for all samples, and the standard deviation is around 1%. To calculate the effective scattering of the stock sample, the volume concentration of the scatterers of each sample was used as the divisor. Again, a good agreement of the determined effective scattering coefficient was found.

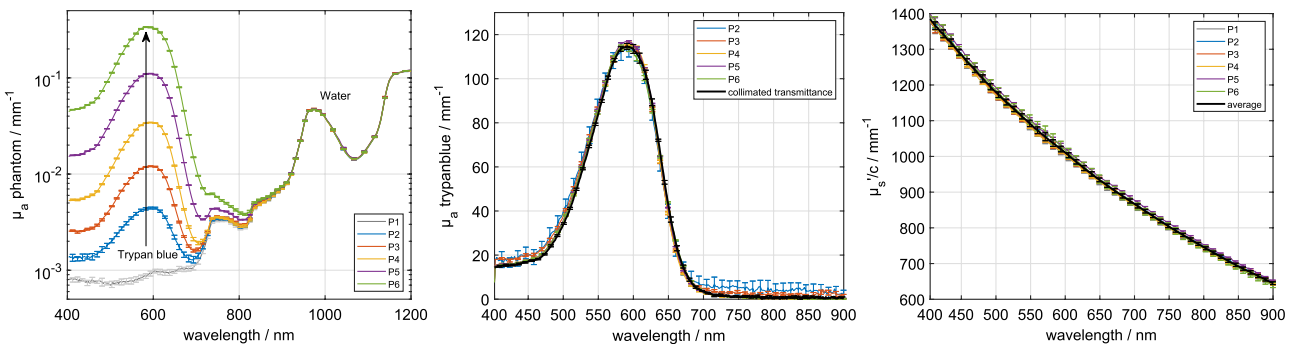


**Fig. 10.** Investigation of the dynamic range of the integrating sphere system using trypan blue as a molecular absorber and the aluminum oxide nanoparticles as scatterers. The absorption coefficient is depicted on the left as well as in the middle, whereas the reduced scattering coefficient is depicted on the right.

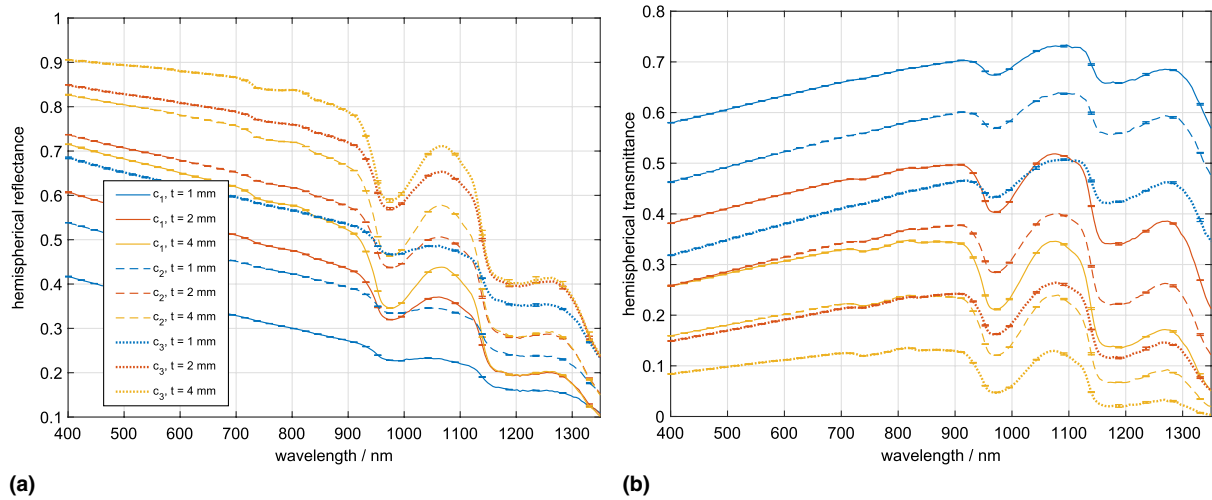


**Fig. 11.** Total hemispherical reflectance (a) and total hemispherical transmittance (b) of the three different concentrations  $c$ , measured with three different sample thicknesses  $t$  using three repetitions at different positions.

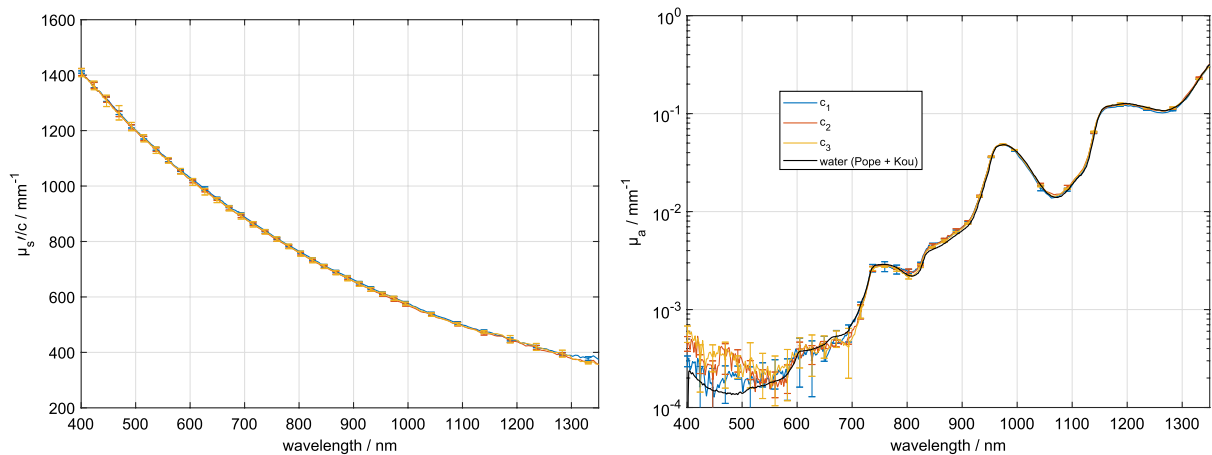


**Fig. 12.** Optical properties of the liquid phantoms based on water and aluminum oxide nanoparticles using different concentrations and different sample thicknesses.

### C. Validation Using Different Sample Thicknesses and Nanoparticle Concentrations

Another important verification was done by using an identical homogeneous sample with different sample thicknesses as well as for a constant sample thickness using different concentrations of scatterers. This examines the precise determination of the optical properties using our method for different thicknesses and different concentrations. We again applied the aluminum oxide nanoparticles suspended in water and filled in cuvettes. The different sample thicknesses were around 1 mm, 2 mm, and 4 mm, whereby the thickness could change slightly by sliding the cover glass plate over the sample compartment, and therefore, the thickness was measured after each sample preparation. Different volume concentrations of  $c_1 = 1.1e-3$  vol%,  $c_2 = 2.1e-3$  vol%, and  $c_3 = 4.5e-3$  vol% resulted in an effective scattering coefficient of about  $\mu'_s = 1, 2.5,$  and  $5 \text{ mm}^{-1}$  at 600 nm. All samples were prepared using an ultrasonic bath for 20 min, and each sample was measured three times at different positions. The measured total hemispherical reflectance

and total hemispherical transmittance are depicted in Fig. 11 and show values between almost zero and 0.9 for the different concentrations and different thicknesses. For the evaluation of the measurements again the refractive index of water, given by Kedenburg, and an approximated asymmetry factor of 0.95 were applied. In Fig. 12, the optical properties of the samples of different thicknesses and identical concentrations are averaged and the effective scattering is divided by the volume concentration of the scatterers. The effective scattering of the stock solution is the same as obtained from the measurement including trypan blue. Furthermore, we found that the effective scattering and absorption coefficients of one concentration using different thicknesses agree well. The relative standard deviation is around 0.5% in  $\mu'_s$  and around 2% in  $\mu_a$  for the VIS range, except for  $\mu_a < 1e-3 \text{ mm}^{-1}$ . Note that the samples with a thickness of 1 mm are not suitable to determine absorption values of  $\mu_a < 5e-2 \text{ mm}^{-1}$  for  $\mu'_s \approx 1 \text{ mm}^{-1}$ , as the optical path length is too short to give information about the absorption, and so the evaluation was ignored in the range of 400–700 nm. The small optical path length of the 1 mm sample is also the

reason for the larger relative standard deviation compared to the samples having a larger thickness or a larger effective scattering. Comparing  $\mu_a$  to our previous validation using polystyrene spheres, we found the same characteristics. Especially, a small discrepancy similar to the literature of Pope *et al.* and Kou *et al.* was obtained. We neglect the evaluation results of the samples having a 4 mm thickness for wavelengths longer than 1315 nm due to the too low transmittance signal. Nevertheless, the overall results are consistent for different thicknesses and different concentrations, and we can conclude that our integrating sphere system delivers trustworthy results and is well verified.

#### 4. ERROR ANALYSIS

Due to an unprecise knowledge of the refractive index  $n$  or the scattering phase function of the investigated turbid media, the obtained scattering and absorption coefficients may be wrongly determined as stated in the first of these two papers [15]. A possible approach is to conduct additional experiments to overcome these limitations such as measurements with a spectrally resolved Abbe refractometer [33] ( $n$ ), with a goniometer [34], or with a collimated transmittance setup (the latter two for characterizing the scattering phase function). Another uncertainty for solving the inverse problem is the surface roughness of solid samples. The influence of the surface roughness was tested experimentally using smooth solid phantoms with thicknesses of 1 mm, 2 mm, and 4 mm based on the epoxy system described by Krauter *et al.* [35] having a  $\mu'_s$  of  $3 \text{ mm}^{-1}$  at 600 nm due to the aluminum oxide nanoparticles mentioned before. The phantoms were sequentially roughened with silicon carbide grinding paper (P180/P320/P600/P1200, Buehler, USA, and P2500/P4000, ATM GmbH, Germany) reaching from macro grits to micro grits by the use of ISO/FEPA grit sizes. After each grinding step, the samples were measured three times with the integrating sphere illuminated at both sides to ensure comparability. The mean thicknesses of the sample slabs were measured at the center to enable a consistent determination of the optical properties. The relative increase in the effective scattering for the sample with 1 mm thickness, when evaluated with the assumption of flat surfaces, was around 10% using the P2500 grid with  $8 \mu\text{m}$  particle diameter and 65% using the P180 grid with  $82 \mu\text{m}$  particle diameter compared to the sample processed with the polishing paste (Acryl und Plexiglas Polierpaste, ROTWEISS, Germany). In Fig. 13, one can see the discrepancy in the optical properties  $\mu'_s$  and  $\mu_a$  depending on the grid sizes of the sandpapers. The smoother the surface, the lower the discrepancy in the optical properties between different thicknesses of the sample. The relative errors in  $\mu'_s$  and  $\mu_a$  due to surface roughness change systematically, comparing different sample thicknesses. Higher optical thicknesses will result in a lower influence due to the lower surface-to-volume scattering fraction. The evaluation was done at two wavelength ranges,  $1200 \pm 5 \text{ nm}$  and  $1300 \pm 5 \text{ nm}$ , to enable the comparison of different absolute  $\mu_a$ . For  $\mu_a = 0.1$  and  $0.01 \text{ mm}^{-1}$ , we found almost comparable deviations in the optical properties. We note that measuring the geometrical sample thickness is a challenge, especially for large surface roughnesses. In order to study the influence of the surface roughness quantitatively, one could perform additional measurements. For example, illuminating

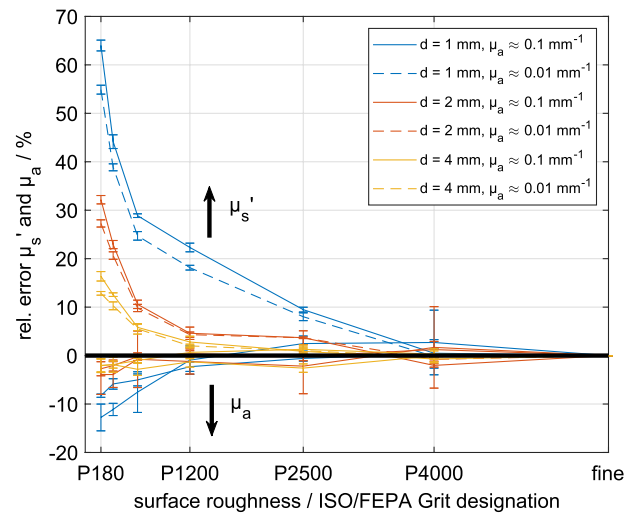


**Fig. 13.** Investigation of the roughness of phantoms based on epoxy resin using sandpapers of different grits and polishing paste (here designated with fine). Two wavelength ranges of the whole spectra were evaluated to enable the comparison of different  $\mu_a = 0.1$  and  $0.01 \text{ mm}^{-1}$ . For rough surfaces, the relative error in  $\mu'_s$  is positive and in  $\mu_a$  negative compared to the sample processed with the polishing paste.

beams having different incident angles, or measurements on identical samples having different thicknesses could be applied. The additional measurements allow to characterize the surface roughness using theoretical surface models such as the generalized Harvey–Shack model [36], which has two surface parameters. Furthermore, a refractive index matching procedure can reduce the surface roughness effects. For this, the sample is placed between two glass slides, and a liquid having a refractive index as close as possible to that of the sample is applied between the sample and the glass slides.

#### 5. SUMMARY

Based on the theoretical integrating sphere considerations discussed in the first paper of this work [15], we showed the results for the determination of the absorption and effective scattering coefficient using the self-made 3D printed integrating sphere. The sphere was covered with a white acrylate universal primer and subsequently coated with  $\text{BaSO}_4$ . For validation of the system, we applied commonly used polystyrene spheres, trypan blue, as well as aluminum nanoparticles to enable the fabrication of homogeneously scattering and absorbing phantoms. We showed consistent results in comparison with Mie's theory and to the stock solution, using different thicknesses of the phantoms. Furthermore, the absorption coefficient of our samples agreed well with the literature. With our method, we can determine precisely the optical properties of turbid media usually with an accuracy for  $\mu'_s$  of around 1% and for  $\mu_a$  of around 3%, for an appropriate optical thickness  $\tau = \mu'_s d > 1$  and an appropriate transmittance signal of  $T > 0.1\%$  in a spectral range of 400 nm to 1500 nm. Furthermore, we performed an experimental error analysis investigating the change of  $\mu'_s$  and  $\mu_a$  due to surface roughness, which may be helpful for many applications.

**Funding.** Deutsche Forschungs Gemeinschaft; Bundesministerium für Wirtschaft und Energie

**Disclosures.** The authors declare that there are no conflicts of interest related to this paper.

## REFERENCES

1. D. Edwards, J. Gier, K. Nelson, and R. Roddick, "Integrating sphere for imperfectly diffuse samples," *J. Opt. Soc. Am.* **51**, 1279–1288 (1961).
2. C. Würth and U. Resch-Genger, "Determination of photoluminescence quantum yields of scattering media with an integrating sphere: direct and indirect illumination," *Appl. Spectrosc.* **69**, 749–759 (2015).
3. J. A. Jacquez and H. F. Kuppenheim, "Theory of the integrating sphere," *J. Opt. Soc. Am.* **45**, 460–470 (1955).
4. J. S. Dam, T. Dalgaard, P. E. Fabricius, and S. Andersson-Engels, "Multiple polynomial regression method for determination of biomedical optical properties from integrating sphere measurements," *Appl. Opt.* **39**, 1202–1209 (2000).
5. M. Friebel, A. Roggan, G. J. Müller, and M. C. Meinke, "Determination of optical properties of human blood in the spectral range 250 to 1100 nm using Monte Carlo simulations with hematocrit-dependent effective scattering phase functions," *J. Biomed. Opt.* **11**, 034021 (2006).
6. J. W. Pickering, C. J. Moes, H. Sterenborg, S. A. Prahl, and M. J. Van Gemert, "Two integrating spheres with an intervening scattering sample," *J. Opt. Soc. Am. A* **9**, 621–631 (1992).
7. A. Roggan, O. Minet, C. Schroeder, and G. J. Mueller, "Determination of optical tissue properties with double integrating sphere technique and Monte Carlo simulations," *Proc. SPIE* **2100**, 42–56 (1994).
8. M. W. Finkel, "Integrating sphere theory," *Opt. Commun.* **2**, 25–28 (1970).
9. L. M. Hanssen and K. A. Snail, "Integrating spheres for mid-and near-infrared reflection spectroscopy," *Handbook Vib. Spectrosc.* **2**, 1175–1192 (2002).
10. J. W. Pickering, S. A. Prahl, N. Van Wieringen, J. F. Beek, H. J. Sterenborg, and M. J. Van Gemert, "Double-integrating-sphere system for measuring the optical properties of tissue," *Appl. Opt.* **32**, 399–410 (1993).
11. A. Roggan, M. Friebel, K. Dörschel, A. Hahn, and G. J. Mueller, "Optical properties of circulating human blood in the wavelength range 400–2500 nm," *J. Biomed. Opt.* **4**, 36–47 (1999).
12. B. Aernouts, E. Zamora-Rojas, R. Van Beers, R. Watté, L. Wang, M. Tsuta, J. Lammertyn, and W. Saeys, "Supercontinuum laser based optical characterization of Intralipid® phantoms in the 500–2250 nm range," *Opt. Express* **21**, 32450–32467 (2013).
13. S. A. Prahl, M. J. van Gemert, and A. J. Welch, "Determining the optical properties of turbid media by using the adding-doubling method," *Appl. Opt.* **32**, 559–568 (1993).
14. A. N. Yaroslavsky, I. V. Yaroslavsky, T. Goldbach, and H.-J. Schwarzmaier, "Influence of the scattering phase function approximation on the optical properties of blood determined from the integrating sphere measurements," *J. Biomed. Opt.* **4**, 47–54 (1999).
15. F. Foschum, F. Bergmann, and A. Kienle, "Precise determination of the optical properties of turbid media using an optimized integrating sphere and advanced Monte Carlo simulations. Part 1: Theory," *Appl. Opt.* **59**, 3203–3215 (2020).
16. J. J. Tomes and C. E. Finlayson, "Low cost 3D-printing used in an undergraduate project: an integrating sphere for measurement of photoluminescence quantum yield," *Euro. J. Phys.* **37**, 055501 (2016).
17. C. Tang, M. Meyer, B. L. Darby, B. Auguie, and E. C. Le Ru, "Realistic ports in integrating spheres: reflectance, transmittance, and angular redirection," *Appl. Opt.* **57**, 1581–1588 (2018).
18. L. M. Hanssen and S. Kaplan, "Infrared diffuse reflectance instrumentation and standards at NIST," *Anal. Chim. Acta* **380**, 289–302 (1999).
19. J. W. Pickering, S. Bosman, P. Posthumus, P. Blokland, J. F. Beek, and M. J. van Gemert, "Changes in the optical properties (at 632.8 nm) of slowly heated myocardium," *Appl. Opt.* **32**, 367–371 (1993).
20. K. A. Snail and L. M. Hanssen, "Integrating sphere designs with isotropic throughput," *Appl. Opt.* **28**, 1793–1799 (1989).
21. J. P. Ritz, A. Roggan, C. T. Germer, C. Isbert, G. Müller, and H. J. Buhr, "Continuous changes in the optical properties of liver tissue during laser-induced interstitial thermotherapy," *Lasers Surg. Med.* **28**, 307–312 (2001).
22. D. Zhu, Q. Luo, and J. Cen, "Effects of dehydration on the optical properties of in vitro porcine liver," *Lasers Surg. Med.* **33**, 226–231 (2003).
23. A. H. Taylor, "The measurement of diffuse reflection factors and a new absolute reflectometer," *J. Opt. Soc. Am.* **4**, 9–23 (1920).
24. S. Babar and J. Weaver, "Optical constants of Cu, Ag, and Au revisited," *Appl. Opt.* **54**, 477–481 (2015).
25. C. Tribastone and W. Peck, "Designing plastic optics: new applications emerging for optical glass substitutes," *The Photonics Design and Applications Handbook* (1998), pp. H426–H433.
26. X. Ma, J. Q. Lu, R. S. Brock, K. M. Jacobs, P. Yang, and X.-H. Hu, "Determination of complex refractive index of polystyrene microspheres from 370 to 1610 nm," *Phys. Med. Biol.* **48**, 4165 (2003).
27. N. Sultanova, S. Kasarova, and I. Nikolov, "Dispersion properties of optical polymers," *Acta Phys. Pol. A* **116**, 585 (2009).
28. R. Michels, F. Foschum, and A. Kienle, "Optical properties of fat emulsions," *Opt. Express* **16**, 5907–5925 (2008).
29. S. Stocker, F. Foschum, P. Krauter, F. Bergmann, A. Hohmann, C. S. Happ, and A. Kienle, "Broadband optical properties of milk," *Appl. Spectrosc.* **71**, 951–962 (2017).
30. S. Kedenburg, M. Vieweg, T. Gissibl, and H. Giessen, "Linear refractive index and absorption measurements of nonlinear optical liquids in the visible and near-infrared spectral region," *Opt. Mater. Express* **2**, 1588–1611 (2012).
31. L. Kou, D. Labrie, and P. Chylek, "Refractive indices of water and ice in the 0.65- to 2.5- $\mu\text{m}$  spectral range," *Appl. Opt.* **32**, 3531–3540 (1993).
32. R. M. Pope and E. S. Fry, "Absorption spectrum (380–700 nm) of pure water. ii. Integrating cavity measurements," *Appl. Opt.* **36**, 8710–8723 (1997).
33. G. Meeten and A. North, "Refractive index measurement of turbid colloidal fluids by transmission near the critical angle," *Measur. Sci. Technol.* **2**, 441 (1991).
34. F. Foschum and A. Kienle, "Optimized goniometer for determination of the scattering phase function of suspended particles: simulations and measurements," *J. Biomed. Opt.* **18**, 085002 (2013).
35. P. Krauter, S. Nothelfer, N. Bodenschatz, E. Simon, S. Stocker, F. Foschum, and A. Kienle, "Optical phantoms with adjustable subdiffusive scattering parameters," *J. Biomed. Opt.* **20**, 105008 (2015).
36. A. Krywonos, "Predicting surface scatter using a linear systems formulation of non-paraxial scalar diffraction," Ph.D. Thesis (2006).